Optical properties of the mouse eye

Ying Geng,[1,2,*] Lee Anne Schery,[1] Robin Sharma,[1,2] Alfredo Dubra,[1,3] Kamran Ahmad,[1] Richard T. Libby,[1,3] and David R. Williams[1,2,3]

[1]*Center for Visual Science, University of Rochester, Rochester, NY, 14627, USA*
[2]*The Institute of Optics, University of Rochester, Rochester, NY, 14620, USA*
[3]*Flaum Eye Institute, University of Rochester, Rochester, NY, 14642, USA*
**ygeng@cvs.rochester.edu*

Abstract: The Shack-Hartmann wavefront sensor (SHWS) spots upon which ocular aberration measurements depend have poor quality in mice due to light reflected from multiple retinal layers. We have designed and implemented a SHWS that can favor light from a specific retinal layer and measured monochromatic aberrations in 20 eyes from 10 anesthetized C57BL/6J mice. Using this instrument, we show that mice are myopic, not hyperopic as is frequently reported. We have also measured longitudinal chromatic aberration (LCA) of the mouse eye and found that it follows predictions of the water-filled schematic mouse eye. Results indicate that the optical quality of the mouse eye assessed by measurement of its aberrations is remarkably good, better for retinal imaging than the human eye. The dilated mouse eye has a much larger numerical aperture (NA) than that of the dilated human eye (0.5 NA vs. 0.2 NA), but it has a similar amount of root mean square (RMS) higher order aberrations compared to the dilated human eye. These measurements predict that adaptive optics based on this method of wavefront sensing will provide improvements in retinal image quality and potentially two times higher lateral resolution than that in the human eye.

©2011 Optical Society of America

OCIS codes: (170.4460) Medical optics and biotechnology: Ophthalmic optics and devices; (330.5370) Vision, color, and visual optics: Physiological optics; (330.4300) Vision system - noninvasive assessment; (110.1080) Active or adaptive optics; (330.7324) Vision, color, and visual optics: Visual optics, comparative animal models.

References and links

1. S. Remtulla and P. E. Hallett, "A schematic eye for the mouse, and comparisons with the rat," Vision Res. **25**(1), 21–31 (1985).
2. C. Schmucker, and F. Schaeffel, "A paraxial schematic eye model for the growing C57BL/6 mouse," Vision Res. **44**(16), 1857–1867 (2004).
3. J. Liang, D. R. Williams, and D. T. Miller, "Supernormal vision and high-resolution retinal imaging through adaptive optics," J. Opt. Soc. Am. A **14**(11), 2884–2892 (1997).
4. D. C. Gray, W. Merigan, J. I. Wolfing, B. P. Gee, J. Porter, A. Dubra, T. H. Twietmeyer, K. Ahamd, R. Tumbar, F. Reinholz, and D. R. Williams, "In vivo fluorescence imaging of primate retinal ganglion cells and retinal pigment epithelial cells," Opt. Express **14**(16), 7144–7158 (2006).
5. D. C. Gray, R. Wolfe, B. P. Gee, D. Scoles, Y. Geng, B. D. Masella, A. Dubra, S. Luque, D. R. Williams, and W. H. Merigan, "In vivo imaging of the fine structure of rhodamine-labeled macaque retinal ganglion cells," Invest. Ophthalmol. Vis. Sci. **49**(1), 467–473 (2008).
6. J. I. Morgan, A. Dubra, R. Wolfe, W. H. Merigan, and D. R. Williams, "In vivo autofluorescence imaging of the human and macaque retinal pigment epithelial cell mosaic," Invest. Ophthalmol. Vis. Sci. **50**(3), 1350–1359 (2008).
7. D. P. Biss, D. Sumorok, S. A. Burns, R. H. Webb, Y. Zhou, T. G. Bifano, D. Côté, I. Veilleux, P. Zamiri, and C. P. Lin, "In vivo fluorescent imaging of the mouse retina using adaptive optics," Opt. Lett. **32**(6), 659–661 (2007).
8. Y. Geng, K. P. Greenberg, R. Wolfe, D. C. Gray, J. J. Hunter, A. Dubra, J. G. Flannery, D. R. Williams, and J. Porter, "In vivo imaging of microscopic structures in the rat retina," Invest. Ophthalmol. Vis. Sci. **50**(12), 5872–5879 (2009).
9. C. Alt, D. P. Biss, N. Tajouri, T. C. Jakobs, and C. P. Lin, "An adaptive-optics scanning laser ophthalmoscope for imaging murine retinal microstructure," Proc. SPIE **7550**, 75501 (2010).
10. P. Artal, P. Herreros de Tejada, C. Muñoz Tedó, and D. G. Green, "Retinal image quality in the rodent eye," Vis. Neurosci. **15**(04), 597–605 (1998).

#139905 - $15.00 USD Received 21 Dec 2010; revised 23 Feb 2011; accepted 24 Feb 2011; published 28 Feb 2011

11. E. L. Irving, M. L. Kisilak, K. M. Clements, and M. C. W. Campbell, "Refractive error and optical image quality in three strains of albino rats," Invest. Ophthalmol. Visual Sci. 46, 000–000 (2005).
12. M. Bird, M. L. Kisilak, and M. C. W. Campbell, "Optical quality of the rat eye," Invest. Ophthalmol. Visual Sci. **48** 000–000 (2007).
13. E. G. de la Cera, G. Rodríguez, L. Llorente, F. Schaeffel, and S. Marcos, "Optical aberrations in the mouse eye," Vision Res. **46**(16), 2546–2553 (2006).
14. O. Lardiere, R. Conan, C. Bradley, K. Jackson, and G. Herriot, "A laser guide star wavefront sensor bench demonstrator for TMT," Opt. Express **16**(8), 5527–5543 (2008).
15. S. L. Polyak, *The vertebrate visual system* (University of Chicago Press., Chicago, 1957).
16. H. Hofer, P. Artal, B. Singer, J. L. Aragón, and D. R. Williams, "Dynamics of the eye's wave aberration," J. Opt. Soc. Am. A **18**(3), 497–506 (2001).
17. J. Liang, B. Grimm, S. Goelz, and J. F. Bille, "Objective measurement of wave aberrations of the human eye with the use of a Hartmann-Shack wave-front sensor," J. Opt. Soc. Am. A **11**(7), 1949–1957 (1994).
18. R. A. Muller and A. Buffington, "Real-time correction of atmospherically degraded telescope images through image sharpening," J. Opt. Soc. Am. **64**(9), 1200–1210 (1974).
19. P. M. Prieto, F. Vargas-Martín, S. Goelz, and P. Artal, "Analysis of the performance of the Hartmann-Shack sensor in the human eye," J. Opt. Soc. Am. A **17**(8), 1388–1398 (2000).
20. A. N. S. Institute, "Methods for Reporting Optical Aberrations of Eyes," in ANSI Z80.28 (2004), pp. 19–28.
21. A. Dubra and Z. Harvey, "Registration of 2D images from fast scanning ophthalmic instruments," in *Biomedical Image Registration*, B. Fischer, B. Dawant, and C. Lorenz, eds. (Springer, Berlin, 2010), pp. 60–71.
22. V. J. Srinivasan, T. H. Ko, M. Wojtkowski, M. Carvalho, A. Clermont, S. E. Bursell, Q. H. Song, J. Lem, J. S. Duker, J. S. Schuman, and J. G. Fujimoto, "Noninvasive volumetric imaging and morphometry of the rodent retina with high-speed, ultrahigh-resolution optical coherence tomography," Invest. Ophthalmol. Vis. Sci. **47**(12), 5522–5528 (2006).
23. M. Ruggeri, H. Wehbe, S. Jiao, G. Gregori, M. E. Jockovich, A. Hackam, Y. Duan, and C. A. Puliafito, "In vivo three-dimensional high-resolution imaging of rodent retina with spectral-domain optical coherence tomography," Invest. Ophthalmol. Vis. Sci. **48**(4), 1808–1814 (2007).
24. O. P. Kocaoglu, S. R. Uhlhorn, E. Hernandez, R. A. Juarez, R. Will, J. M. Parel, and F. Manns, "Simultaneous fundus imaging and optical coherence tomography of the mouse retina," Invest. Ophthalmol. Vis. Sci. **48**(3), 1283–1289 (2007).
25. L. N. Thibos, M. Ye, X. Zhang, and A. Bradley, "The chromatic eye: a new reduced-eye model of ocular chromatic aberration in humans," Appl. Opt. **31**(19), 3594–3600 (1992).
26. E. J. Fernández, A. Unterhuber, P. M. Prieto, B. Hermann, W. Drexler, and P. Artal, "Ocular aberrations as a function of wavelength in the near infrared measured with a femtosecond laser," Opt. Express **13**(2), 400–409 (2005).
27. A. Hughes, "A useful table of reduced schematic eyes for vertebrates which includes computed longitudinal chromatic aberrations," Vision Res. **19**(11), 1273–1275 (1979).
28. C. J. Jeon, E. Strettoi, and R. H. Masland, "The major cell populations of the mouse retina," J. Neurosci. **18**(21), 8936–8946 (1998).
29. E. Soucy, Y. S. Wang, S. Nirenberg, J. Nathans, and M. Meister, "A novel signaling pathway from rod photoreceptors to ganglion cells in mammalian retina," Neuron **21**(3), 481–493 (1998).
30. S. S. Nikonov, R. Kholodenko, J. Lem, and E. N. Pugh, Jr., "Physiological features of the S- and M-cone photoreceptors of wild-type mice from single-cell recordings," J. Gen. Physiol. **127**(4), 359–374 (2006).
31. J. Z. Liang and D. R. Williams, "Aberrations and retinal image quality of the normal human eye," J. Opt. Soc. Am. A **14**(11), 2873–2883 (1997).
32. J. Porter, H. Queener, J. Lin, K. Thorn, and A. Awwal, *Adaptive Optics for Vision Science* (Wiley-Interscience, 2006), pp. 68–69.
33. A. Dubra, "Wavefront sensor and wavefront corrector matching in adaptive optics," Opt. Express **15**(6), 2762–2769 (2007).
34. F. W. Campbell, and D. G. Green, "Optical and retinal factors affecting visual resolution," J. Physiol. **181**(3), 576–593 (1965).
35. R. Sabesan and G. Yoon (Institute of Optics, University of Rochester, Rochester, New York, USA, personal communication).
36. N. Putnam (School of Optometry and Vision Science Graduate Group, University of California, Berkeley, Berkeley, California, USA, personal communication).
37. S. Tuohy and A. G. Podoleanu, "Depth-resolved wavefront aberrations using a coherence-gated Shack-Hartmann wavefront sensor," Opt. Express **18**(4), 3458–3476 (2010).
38. A. Dubra (Flaum Eye Institute, University of Rochester, Rochester,New York, USA, personal communication, 2010).
39. M. Glickstein and M. Millodot, "Retinoscopy and eye size," Science **168**(931), 605–606 (1970).
40. J. Tejedor and P. de la Villa, "Refractive changes induced by form deprivation in the mouse eye," Invest. Ophthalmol. Vis. Sci. **44**(1), 32–36 (2003).
41. V. A. Barathi, V. G. Boopathi, E. P. Yap, and R. W. Beuerman, "Two models of experimental myopia in the mouse," Vision Res. **48**(7), 904–916 (2008).
42. T. V. Tkatchenko and A. V. Tkatchenko, "Ketamine-xylazine anesthesia causes hyperopic refractive shift in mice," J. Neurosci. Methods **193**(1), 67–71 (2010).
43. A. Chaudhuri, P. E. Hallett, and J. A. Parker, "Aspheric curvatures, refractive indices and chromatic aberration for the rat eye," Vision Res. **23**(12), 1351–1363 (1983).

#139905 - $15.00 USD Received 21 Dec 2010; revised 23 Feb 2011; accepted 24 Feb 2011; published 28 Feb 2011
(C) 2011 OSA

44. M. Millodot and J. Sivak, "Hypermetropia of small animals and chromatic aberration," Vision Res. **18**(1), 125–126 (1978).
45. A. Hughes, "The artefact of retinoscopy in the rat and rabbit eye has its origin at the retina/vitreous interface rather than in longitudinal chromatic aberration," Vision Res. **19**(11), 1293–1294 (1979).
46. K. R. Huxlin, G. Yoon, L. Nagy, J. Porter, and D. Williams, "Monochromatic ocular wavefront aberrations in the awake-behaving cat," Vision Res. **44**(18), 2159–2169 (2004).
47. F. Schaeffel, E. Burkhardt, H. C. Howland, and R. W. Williams, "Measurement of refractive state and deprivation myopia in two strains of mice," Optom. Vis. Sci. **81**(2), 99–110 (2004).
48. M. Choi, S. Weiss, F. Schaeffel, A. Seidemann, H. C. Howland, B. Wilhelm, and H. Wilhelm, "Laboratory, clinical, and kindergarten test of a new eccentric infrared photorefractor (PowerRefractor)," Optom. Vis. Sci. **77**(10), 537–548 (2000).
49. A. Roorda, M. C. Campbell, and W. R. Bobier, "Geometrical theory to predict eccentric photorefraction intensity profiles in the human eye," J. Opt. Soc. Am. A **12**(8), 1647–1656 (1995).
50. A. Roorda, M. C. Campbell, and W. R. Bobier, "Slope-based eccentric photorefraction: theoretical analysis of different light source configurations and effects of ocular aberrations," J. Opt. Soc. Am. A **14**(10), 2547–2556 (1997).
51. L. Gianfranceschi, A. Fiorentini, and L. Maffei, "Behavioural visual acuity of wild type and bcl2 transgenic mouse," Vision Res. **39**(3), 569–574 (1999).
52. G. T. Prusky and R. M. Douglas, "Developmental plasticity of mouse visual acuity," Eur. J. Neurosci. **17**(1), 167–173 (2003).
53. C. Schmucker, M. Seeliger, P. Humphries, M. Biel, and F. Schaeffel, "Grating acuity at different luminances in wild-type mice and in mice lacking rod or cone function," Invest. Ophthalmol. Vis. Sci. **46**(1), 398–407 (2005).
54. J. D. Pettigrew, B. Dreher, C. S. Hopkins, M. J. McCall, and M. Brown, "Peak density and distribution of ganglion cells in the retinae of microchiropteran bats: implications for visual acuity," Brain Behav. Evol. **32**(1), 39–56 (1988).
55. U. C. Dräger and J. F. Olsen, "Ganglion cell distribution in the retina of the mouse," Invest. Ophthalmol. Vis. Sci. **20**(3), 285–293 (1981).
56. L. Llorente, L. Diaz-Santana, D. Lara-Saucedo, and S. Marcos, "Aberrations of the human eye in visible and near infrared illumination," Optom. Vis. Sci. **80**(1), 26–35 (2003).
57. G. A. Horridge, "The compound eye of insects," Sci. Am. **237**(1), 108–120 (1977).
58. A. W. Snyder, S. B. Laughlin, and D. G. Stavenga, "Information capacity of eyes," Vision Res. **17**(10), 1163–1175 (1977).
59. A. W. Snyder, T. R. J. Bossomaier, and A. Hughes, "Optical image quality and the cone mosaic," Science **231**(4737), 499–501 (1986).
60. W. M. Harmening, M. A. Vobig, P. Walter, and H. Wagner, "Ocular aberrations in barn owl eyes," Vision Res. **47**(23), 2934–2942 (2007).
61. W. M. Harmening, P. Nikolay, J. Orlowski, and H. Wagner, "Spatial contrast sensitivity and grating acuity of barn owls," J. Vis. **9**(7), 13 (2009).
62. M. W. Seeliger, S. C. Beck, N. Pereyra-Muñoz, S. Dangel, J. Y. Tsai, U. F. Luhmann, S. A. van de Pavert, J. Wijnholds, M. Samardzija, A. Wenzel, E. Zrenner, K. Narfström, E. Fahl, N. Tanimoto, N. Acar, and F. Tonagel, "In vivo confocal imaging of the retina in animal models using scanning laser ophthalmoscopy," Vision Res. **45**(28), 3512–3519 (2005).
63. M. Paques, M. Simonutti, M. J. Roux, S. Picaud, E. Levavasseur, C. Bellman, and J. A. Sahel, "High resolution fundus imaging by confocal scanning laser ophthalmoscopy in the mouse," Vision Res. **46**(8-9), 1336–1345 (2006).
64. M. K. Walsh and H. A. Quigley, "In vivo time-lapse fluorescence imaging of individual retinal ganglion cells in mice," J. Neurosci. Methods **169**(1), 214–221 (2008).
65. C. K. Leung, J. D. Lindsey, J. G. Crowston, C. Lijia, S. Chiang, and R. N. Weinreb, "Longitudinal profile of retinal ganglion cell damage after optic nerve crush with blue-light confocal scanning laser ophthalmoscopy," Invest. Ophthalmol. Vis. Sci. **49**(11), 4898–4902 (2008).
66. G. J. McCormick, J. Porter, I. G. Cox, and S. MacRae, "Higher-order aberrations in eyes with irregular corneas after laser refractive surgery," Ophthalmology **112**(10), 1699–1709 (2005).

1. Introduction

The mouse is frequently adopted as the model system for investigating the normal and diseased eye because it is inexpensive, reproduces and matures rapidly, and is amenable to genetic manipulations that are not yet possible in other mammals. Despite its widespread use in vision research, relatively little quantitative information is available about the optics of the mouse eye. A few schematic eyes for the mouse have been proposed [1,2]. These incorporate the large spherical crystalline lens that fills most of the ocular volume and an axial length of about 3.3 mm, 8 times smaller than that of the human eye. Consistent with the mouse's nocturnal habit, its eye has a numerical aperture (NA) of about 0.49 when the pupil is fully dilated, about two times greater than that of the human eye.

#139905 - $15.00 USD Received 21 Dec 2010; revised 23 Feb 2011; accepted 24 Feb 2011; published 28 Feb 2011
(C) 2011 OSA

Knowledge of the optical aberrations of the mouse eye is important not only for understanding the visual capabilities of the mouse, but also because correcting these aberrations can improve the quality of *in vivo* images of the mouse retina. *In vivo* imaging offers the advantage over post mortem histology of tracking in individual animals developmental changes, disease progression, or the efficacy of therapy. This can reduce the number of animals required and the animal to animal variability inherent in constructing the dynamics of a process from different animals sacrificed at different time points. The optical aberrations of the mouse eye can be corrected with adaptive optics (AO), which has enabled diffraction-limited imaging of cellular and sub-cellular structures in the living human and primate eyes [3–6]. Recently, a few pilot studies have demonstrated that some of the benefits of AO found in primates can be realized in rodent eyes [7–9]. However, most investigations that have attempted to measure the optical quality of the rodent eye have concluded either that it is poor or have encountered technical difficulties in measuring it. One study found very poor retinal image quality in both the rat and the mouse using the double pass method [10]. With the development of wavefront sensing, it is now possible to directly measure aberrations in rodent eyes. Irving et al. and Bird et al. showed distorted spots and qualitative wave aberration measurements in rat eyes using a Shack-Hartmann wavefront sensor (SHWS) [11,12]. A recent study measured wave aberrations up to the 4th order Zernikes over a 1.5 mm pupil in the mouse eye, showing clearly more degraded Shack-Hartman spots than that of the typical human eye [13].

Biss et al. found it difficult to measure the wavefront using back-scattered light due to very large wavefront sensor spots [7]. To avoid this poor spot quality, they used the fluorescence signal from a single layer of labeled retinal cells rather than back-scattered light for wavefront sensing. This is a clever solution, but it has the limitations that the signal available for wavefront sensing is reduced by an order of magnitude or more and requires the use of intrinsic or extrinsic fluorophores, which may not be available or feasible depending on the experiment. In the rat eye, we observed similar difficulties with backscattered light but found that the wavefront sensor spots were good enough to correct aberrations with an AO control loop, enabling sub-cellular imaging of ganglion cell axons and dendrites [8].

The inferior SHWS spot quality in rodent eyes is caused by the fact that the wavefront sensing beacon is reflected from multiple layers of the optically thick retina. This phenomenon is similar to the elongation of wavefront sensor spots from artificial guide stars in astronomy. In that case, elongation is caused by the thickness of the sodium layer in the atmosphere that is illuminated with a ground-based laser to produce the wavefront sensor beacon [14]. In the mouse eye (see Fig. 1), the SHWS spots are often elongated radially, with the axis of elongation typically pointing toward the point where the laser beacon enters the pupil of the eye. Figure 1 shows an image of the lenslet array superimposed on the eye's pupil to illustrate this point using only a single line of lenslets. When the light from the

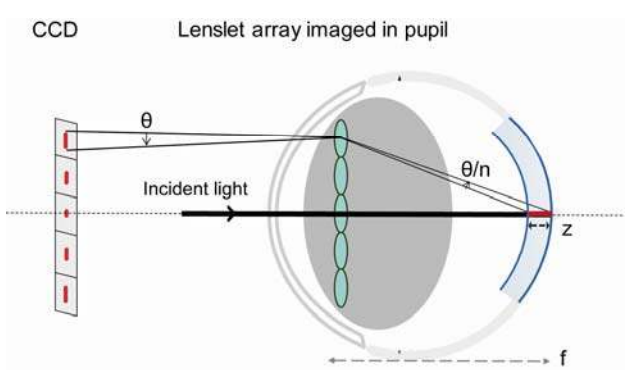

Fig. 1. Schematic explaining the elongation of wavefront sensor spots in the mouse eye. θ: elongation angle. n: refractive index of the retina. Note that the lenslets are in a plane conjugate to the eye's pupil, and not physically on it.

#139905 - $15.00 USD Received 21 Dec 2010; revised 23 Feb 2011; accepted 24 Feb 2011; published 28 Feb 2011
(C) 2011 OSA

beacon is reflected from the retina (shown in red), all the lenslets imaging the illuminated part of retina off-axis with respect to the illuminating beam will produce a radially elongated spot image, with increasing amounts of elongation the further off-axis the lenslet happens to be. If there are two layers that have the brightest back reflections from the retina (shown in blue), as is often the case to a first approximation, a double spot pattern will appear in the raw wavefront image. The spot arising from the more posterior of the two surfaces lies closer to the illumination axis than the spot arising from the more anterior surface. This double spot pattern will be discussed in more detail later.

For a lenslet at the edge of the pupil, the amount of elongation of its wavefront sensor spot can be described by an elongation angle θ, which can be approximated below in Eq. (1). Here *NA* is the eye's numerical aperture, *z* is the largest axial separation between reflecting layers or the retinal thickness, and *f* is the focal length of the eye.

$$\theta \approx NA\frac{z}{f} \tag{1}$$

If there is no magnification factor between the eye's pupil and the pupil plane of the wavefront sensor, then the angle of elongation for the wavefront sensor spot on the edge of the pupil θ' is the same as θ. If the eye's pupil is magnified to the wavefront sensor pupil, the largest angle of elongation on the wavefront sensor θ' becomes:

$$\theta' = \frac{D_e}{D_w}\theta \approx \frac{D_e}{D_w}NA\frac{z}{f} \tag{2}$$

where D_e is the eye's pupil size and D_w is the pupil size of the wavefront sensor.

Table 1 summarizes a few example calculations made for the elongation angle of a mouse eye versus a human eye. Equation (1) makes it immediately clear that there are at least two reasons why the wavefront sensor spot quality is so much poorer in the mouse eye than in the human. First, the mouse eye has a larger NA (0.49 for a 2 mm pupil vs. 0.18 for a human 6 mm pupil). Second, it has a larger retinal thickness when expressed relative to the eye's focal length, z/f. It is approximately 9% for the mouse vs. 1.7% for the thickest part of the human retina, and 0.6% for the thinnest part of the human retina. Thus the elongation angle θ in the mouse retina is 15 times larger than that of the human extrafoveal retina at its thickest point, and over 40 times larger than that of the human foveal center.

Table 1. Elongation angle calculated for the mouse eye vs. the human eye*

Retina	Pupil size	$\frac{D_e}{D_w}$	NA	*f*	*z*	*z/f*	θ'	$\frac{\theta'_{Mouse}}{\theta'_{Human}}$
Mouse average	2 mm	1	0.49	2.6 mm	230 µm	9%	2.51°	15 – 42
		0.33					0.84°	5 – 14
Human thinnest	6 mm	1	0.18	22.3 mm	130 µm	0.6%	0.06°	
Human thickest					370 µm	1.7%	0.17°	

*Mouse eye *f* and *z* are values for the adult mouse eye [2]. Human eye *f* is from the Gullstrand-Le Grand model and *z* is from Polyak [15]. Values for D_e / D_W are example values.

If there is magnification between the eye's and the wavefront sensor's pupil, then Eq. (2) is used to calculate the elongation angle on the wavefront sensor spots. For example, if both the human pupil and the mouse pupil are imaged onto the same human pupil size on the wavefront sensor, D_w is the same for both species. Then the elongation angle θ' calculated

#139905 - $15.00 USD Received 21 Dec 2010; revised 23 Feb 2011; accepted 24 Feb 2011; published 28 Feb 2011
(C) 2011 OSA

using the same parameters in the previous paragraph will be 5 to 14 times larger in the mouse eye than in the human eye.

The elongation of the wavefront sensor spots will introduce error into the estimate of the wave aberration to the extent that it displaces the centroid computed for each spot. If the only difference between the light reflected from different retinal layers was a difference in axial position, one might expect that their only effect would be on the defocus term of the wave aberration. However, in our experience, light from each retinal layer can produce its own idiosyncratic light distribution in the pupil. This means that light from a particular layer may have more effect on the centroid in one part of the pupil than another, further complicating the irregularities in the wavefront sensor spots across the pupil, and introducing spurious aberrations in the wavefront sensor estimate that do not exist in the anterior optics of the eye. By capitalizing on a few simple optical principles we can mitigate the influence on wavefront sensing of light backscattered from multiple layers. This way we have measured the wave aberration in the mouse eye over a fully dilated pupil up to 10th order Zernike polynomials and have explored the implications of these aberrations especially for microscopic imaging of the retina in the living eye.

2. Methods

2.1 Subjects

Ten black C57BL/6J wild type mice from 2 months to 5 months of age were used in wave aberration measurement experiments, and the same mice from 7 months to 9 months of age were used in the chromatic aberration study. Mice were housed in standard mouse cages under 12 hour light/dark cycle. All animals were handled according to the Association for Research in Vision and Ophthalmology Statement for the Use of Animals in Ophthalmic and Vision Research and to the guidelines of the University Committee on Animal Resources at the University of Rochester.

2.2 The Shack-Hartmann wavefront sensor for the mouse eye

A SHWS was constructed for the mouse eye and the schematic layout of the system is shown in Fig. 2. A single mode fiber-coupled 789 nm superluminescent diode (SLD) with 11.5 nm bandwidth (InPhenix, Livermore, CA USA) was used as the wavefront sensing light source. The SLD's fiber connector was mounted on a translation stage so that the light source could be focused at different planes in the retina. The wavefront sensor consisted of a lenslet array (Adaptive Optics Associates, Cambridge, MA USA) with 18 mm focal length and 325 μm lenslet pitch, and a 1004x1004 pixel CCD camera (Cohu, San Diego, CA USA). Wave aberrations were measured using back scattered light at 10Hz.

The optical path consisted of three pupil planes (a wavefront sensor pupil plane, a plane for inserting trial lenses, and a plane for a resonant scanner) conjugate to the eye's pupil using off axis spherical mirror 4-f telescopes. Defocus and astigmatism could be corrected at the trial lens plane, but for this study it was not used when aberration data were measured. Speckle in the wavefront sensing spot images was reduced by the wide bandwidth SLD and was further reduced by the resonant scanner (Electro-Optical Products Corp, Glendale, NY USA) which line-scanned the retina at 15 kHz [16]. In comparison, the CCD camera exposure time typically used was 5 ms to 50 ms. The scanning angle on the eye's pupil was kept smaller than 0.5 degrees. To monitor the pupil centration and the eye's rotation, the mouse pupil was illuminated with an infrared (IR) light emitting diode (LED) ring and imaged onto a CCD camera (The Imaging Source LLC., Charlotte, NC USA). A simple fundus camera consisting of an LED light source (Thorlabs Inc., Newton, NJ USA) and a CMOS camera (NET USA INC., Highland, IN USA) monitored the retinal location during measurement.

#139905 - $15.00 USD Received 21 Dec 2010; revised 23 Feb 2011; accepted 24 Feb 2011; published 28 Feb 2011
(C) 2011 OSA

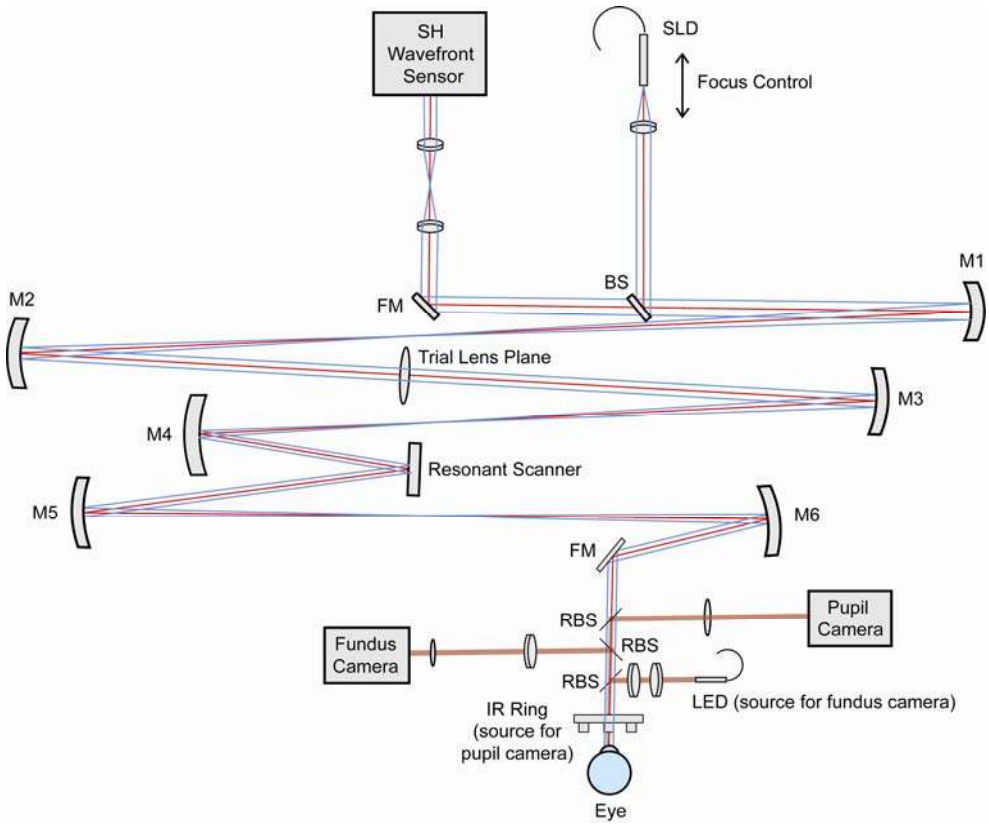

Fig. 2. Schematic of the mouse eye wavefront sensor. SLD: fiber coupled Super Luminescent Diode. SH Wavefront Sensor: Shack-Hartmann wavefront sensor. BS: Beam Splitter. RBS: Removable Beam Splitter. FM: Fold Mirror. M1-6: Concave spherical Mirrors.

2.3 Experiment design

Mice were anesthetized using a ketamine (~65 mg/kg) and xylazine (~8 mg/kg) cocktail and covered by a heating pad during measurement. Pupils were dilated with one drop of 2.5% phenylephrine (Neo-Synephrine) and one drop of 0.5% tropicamide.

Mice were stabilized on a bitebar stage with two rotational degrees of freedom (Bioptigen, Research Triangle Park, NC USA). The bitebar stage was mounted on a three-axis translation stage to align the center of rotation of the bitebar stage with the exit pupil of the wavefront sensor. The bite bar itself could be translated in two dimensions to align the mouse eye pupil to the center of rotation of the stage. Then the stage could be rotated to measure different retinal locations without misalignment of the pupil.

The pupil camera provided easy alignment and monitoring of the pupil position. The bitebar stage was rotated so that the first Purkinje image from the IR illuminator ring was centered on the eye's pupil. To measure along the optical axis, the optic disk was found with the fundus camera. Wave aberration measurements were usually performed near the optic disk (at 4° temporal unless described otherwise). The cornea was periodically lubricated with saline solution to prevent dehydration. After each saline drop, the excess was carefully removed with a cotton swab, and 10 images were collected. The same procedure was repeated at least 6 times, yielding over 60 images to average for each eye.

2.4 Wavefront spot image collection

In the current configuration, a total of 321 lenslets were used to sample a 2 mm pupil, and 44x44 CCD pixels were used for each lenslet. The Shack-Hartmann spot positions obtained

#139905 - $15.00 USD Received 21 Dec 2010; revised 23 Feb 2011; accepted 24 Feb 2011; published 28 Feb 2011
(C) 2011 OSA

with the mouse eye were always referenced to spot positions obtained when the eye was replaced with a point source in the back focal plane of a long focal length (140 mm EFL), high quality achromatic doublet placed where the eye's pupil would have been. The use of this reference allowed the wave aberration measurements of the mouse eye to be unaffected by any aberrations intrinsic to the wavefront sensor.

For wavefront sensing in the human eye, especially in commercial instruments, a small diameter illumination beam is typically used to increase the depth of focus, so that the wavefront sensor spots are less susceptible to focus and aberration artifacts on the first pass into the eye [17]. However, in the mouse eye, the increased depth of focus provided by a small diameter beam exacerbates the problem of multiple back reflections from multiple retinal layers. When a narrow beam is used as the illumination beam, we often see two patterns of sharp spots superimposed. The two spot patterns follow a similar radial elongation pattern shown in Fig. 1. Their separations are largest at the edge of pupil and are superimposed at the point of beam entry. To reduce the depth of focus, we used the largest diameter beacon we could, 2 mm outer diameter which nearly filled the eye's pupil. (The depth of focus is ~3 μm for a diffraction-limited mouse eye with a 2 mm pupil size and 0.49 NA.) To avoid back reflections from the first surface of the cornea and possibly from the posterior surface of the lens, an annular beacon with 0.3 mm inner diameter was used. The beacon was then focused on the retinal layer of interest, and due to the small depth of focus, light from distant unwanted retinal layers was blurred thus reducing its influence on the centroid. The best focus of the beacon could be found in either of two ways: subjectively by translating the beacon while observing the sharpness change of the wavefront spots, or objectively by using an automated metric to find the sharpest spots. In the current study we did this objectively by using a simple sharpness metric [18]. To remove its dependence on the overall spot intensity of the Shack-Hartmann image, we normalized the metric as shown in Eq. (3). This normalized sharpness metric S was computed for the wavefront spot pattern in real time to help find the sharpest spots which corresponded to the best focus position. It calculates the normalized intensity square for all the pixels in the entire Shack-Hartmann spot image, and yields a larger number for an image with a sharper overall spot pattern.

$$S = \frac{\sum_{\text{SH image}} I_{i,j}^2}{\left[\sum_{\text{SH image}} I_{i,j}\right]^2} \tag{3}$$

where x, y are coordinates in the Shack-Hartmann spot image, and $I(x,y)$ is the spot intensity.

2.5 Wave aberration data analysis

As mentioned previously, spurious back reflections from multiple layers can make the wavefront sensing spots quite asymmetric for the mouse eye. Therefore, in addition to decreasing the depth of focus, we chose to process the wavefront sensor images in a way that reduced the impact of asymmetries in each spot image on the aberration estimate. For centroiding the wavefront spots, an iterative window size center of mass algorithm was used [19]. To further diminish possible contributions of light from unwanted retinal layers, the final window size was set at 1/4 of the diffraction-limited spot Airy-disk size. This was done because measurements showed that aberration coefficients reach an asymptotic level at window sizes at or smaller than ~1/4 of the airy-disk size. This, along with the observation that the spot profiles appeared symmetric over these small windows, suggests that the influence of other retinal layers was largely eliminated.

Additionally, in order to capture the large differences in refractive error of individual mice and different retinal layers within the same mouse, the centroiding algorithm required an additional feature. This was accomplished by roughly centering the initial search window positions on the spots using the estimated amount of defocus, thereby increasing the dynamic range of the wavefront sensor.

#139905 - $15.00 USD Received 21 Dec 2010; revised 23 Feb 2011; accepted 24 Feb 2011; published 28 Feb 2011
(C) 2011 OSA

The wave aberration was expressed as a combination of Zernike polynomials up to and including 10th order according to the ANSI standards [20]. The Zernike coefficients calculated from the 10 images obtained after each saline drop have very low variability, thus these images are averaged before averaging data from image sets acquired after different saline drops. The variability in the wave aberration measurements is indicative of the variation between administrations of saline drops. Wave aberrations measured over a large pupil size were sometimes truncated and renormalized to a smaller pupil size for analysis. Strehl ratios and modulation transfer functions (MTFs) were calculated from the wave aberration data.

2.6 Chromatic aberration measurement

One of our goals was to measure the refractive state of the mouse eye, which requires correcting the wave aberration measurements obtained in IR light for the chromatic aberration of the mouse eye. To measure chromatic aberration, the mouse eye's spherical equivalent values were measured through wavefront sensing using four different wavelengths (457 nm, 514 nm, 633 nm, 789 nm). Besides the wavefront sensing SLD that has a central wavelength of 789 nm, an air-cooled Argon laser (CVI Melles Griot, Albuquerque, NM USA) provided two lines at 457 nm and 514 nm. A He-Ne laser (CVI Melles Griot, Albuquerque, NM USA) was used to measure the wavefront at 633 nm. Measurements were performed on the optic disk of 9 mouse eyes over a 2 mm pupil diameter. The focus control of the wavefront sensing beacon mount was adjusted for each wavelength so that the beacon is focused on the layer of interest and the wavefront spots are sharp. For each wavelength and each eye, a minimum of 4 measurements were averaged. To minimize variability of the wavefront over time caused by factors including dissipation of eye drops and slow eye movements, each measurement made with a visible wavelength was paired with an adjacent reference measurement made with 789 nm. No eye drops were applied between the two measurements. The refractive error differences between each visible wavelength and the reference wavelength were recorded and averaged for all eyes.

2.7 OCT imaging

A Bioptigen OCT system (Bioptigen, Research Triangle Park, NC USA) was used to collect OCT images in the mouse eye. The light source of the OCT system has a central wavelength of 860 nm and a bandwidth of 130 nm. Mice were anesthetized and dilated the same way as stated in section 2.3. A custom made rigid contact lens (Unicon Corporation, Osaka, Japan) was placed on the eye to maintain corneal hydration. Line scan images were registered and averaged to increase signal to noise using a custom-written algorithm [21].

2.8 Retinal image simulation

To better understand the implications of the mouse wave aberration for the quality of retinal images, we simulated the retinal image quality that could be achieved under ideal incoherent imaging conditions with and without AO correction. Note that this simulation doesn't account for scattering, photon noise and other sources of noise that degrade retinal image quality. The optical transfer function (OTF) of the system can be calculated using typical higher order aberration data measured in a mouse eye. The Fourier transform of the OTF is the point spread function (PSF). By convolving an original image with the PSF, an *in vivo* retinal image taken under best conditions without using AO was simulated. By convolving the original image with a diffraction-limited PSF, an image with ideal AO correction in the absence of noise was simulated.

3. Results

3.1 Shack-Hartmann image quality

The typical poor quality of mouse Shack-Hartmann wavefront images is illustrated in Fig. 3 [13]. Figure 3(a) shows a 3x3 array of spots taken from a wavefront sensor raw image obtained by using an SLD beacon that filled the whole pupil, without optimizing the focus of

#139905 - $15.00 USD Received 21 Dec 2010; revised 23 Feb 2011; accepted 24 Feb 2011; published 28 Feb 2011
(C) 2011 OSA

the beacon. The spots are large and blurry, demonstrating a cross-section that has a bimodal appearance. An OCT scan of the mouse retina also shows that the strongest back reflections come generally from two components: the inner retina and from the outer retina, with a distinctly less reflective region in between (Fig. 3(b)). This is particularly clear in linear plots of the OCT signal vs. depth since the logarithmic representation used ubiquitously in OCT images reduces the large differences in the reflectance of different layers. We use the term outer retina loosely here because we have not undertaken a detailed analysis of which specific layers contribute most to this light. OCT images of mouse published elsewhere tend to suggest major contributions from the retinal pigment epithelium (RPE) and choroid [22,23]. Back reflections from the inner retina have a large variability with retinal location and are not as

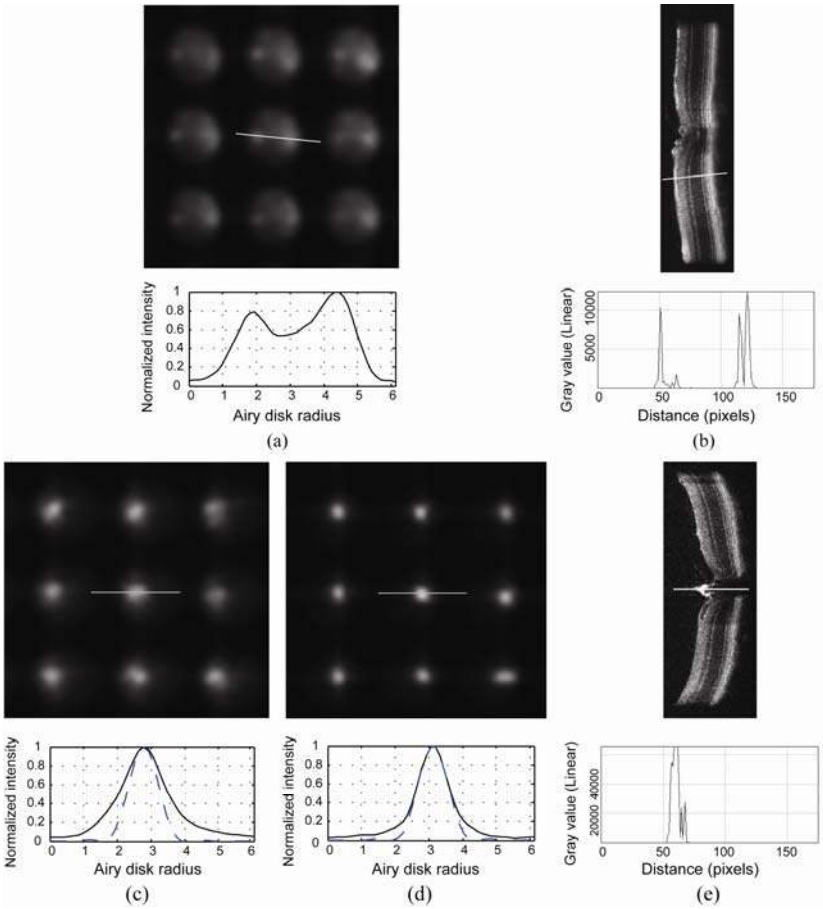

Fig. 3. (a) Typical non-optimized wavefront sensor spot pattern in the mouse eye with a cross section of a single spot shown below. (b) An OCT line scan image with a cross section on a particular retinal location. OCT signal vs. depth for the cross section is shown below in linear scale. Both the wavefront spots and the OCT image show back reflections from two major layers from the retina. (c) Improved wavefront spots when the beacon is focused on the outer retina, when source focus was set at ~-10 D. Cross section of a single spot is shown below. Solid line: normalized intensity profile for the cross section. Dashed line: diffraction-limited spot profile for a lenslet. (d) An even sharper spot pattern can be obtained when the beacon is focused on the disk, when the source focus was set at ~20 D. Cross section of a single spot is shown below. Solid line: normalized intensity profile for the cross section. Dashed line: diffraction-limited spot profile for a lenslet. The wavefront sensor spots are very close to diffraction-limited. (e) An OCT line scan image taken on the optic disk with a cross section on the central retinal artery. OCT signal vs. depth for the cross secion is shown below in linear scale.

#139905 - $15.00 USD Received 21 Dec 2010; revised 23 Feb 2011; accepted 24 Feb 2011; published 28 Feb 2011
(C) 2011 OSA

uniform as that from the deeper layers. Some of the back reflections have a specular reflection component that could originate from blood vessels, nerve fibers or the vitreal retinal interface. This direction dependent back reflection from the inner retina results in an asymmetric wavefront spot pattern that may further degrade the accuracy of aberration measurement.

By optimizing the focus of the wavefront sensing beacon, the spot quality can be improved significantly. Figure 3(c) shows that for the same entry beam diam eter (2 mm), by changing the beacon focus by ~-10 diopters so that the outer retina is in focus, a relatively symmetric single spot pattern can be obtained. An even better and brighter spot pattern was obtained at the optic disk (Fig. 3(d)), presumably generated by reflection from the central retinal artery that shows up in an OCT image taken on the disk (shown in Fig. 3(e)) [24]. Source focus was at ~20 diopters for the spots obtained at the disk. Dashed lines in Fig. 3(c) and Fig. 3(d) are the diffraction-limited spot profile for each lenslet. Figure 3(d) shows that on the optic disk (central retinal artery), where the retina's multilayer reflection is absent, the mouse eye wavefront sensor spots we recorded were very close to diffraction-limited.

3.2 Refractive state

Two different refractive states were obtained by analyzing the spot pattern focused on the outer retina vs. the inner retina. The average measured values are shown in Fig. 4. for two different pupil sizes, a dilated pupil diameter of 2 mm, and a smaller pupil diameter of 0.8 mm. 18 eyes were measured on the optic disk, and the spherical equivalent was consistently hyperopic for all eyes, with a value of + 21.3 ± 1.3 D (mean ± 2 SEM (Standard Error of the Mean)) for a 2 mm pupil, and + 23.2 ± 4.5 D for a 0.8 mm pupil. 20 eyes were measured with the focus at the outer retina, and all the eyes were myopic with the exception of one eye, with an average spherical equivalent of −7.4 ± 1.8 D for a 2 mm pupil, and −11.1 ± 3.7 D for a 0.8 mm pupil.

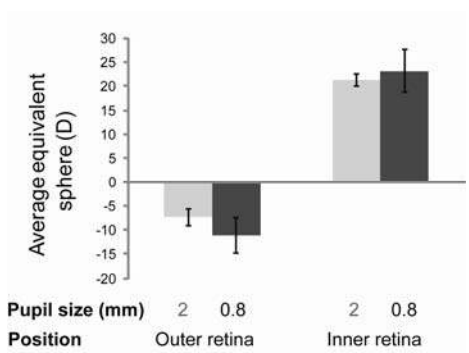

Fig. 4. Average equivalent sphere of mice eyes measured in two different positions over two pupil sizes. Left column: spherical equivalent measured on the outer retina. Right column: spherical equivalent measured on the inner retina. Light gray bars: spherical equivalent for 2 mm pupil size. Dark gray bars: spherical equivalent for 0.8 mm pupil size. Error bar: ± 2 times SEM.

3.3 Chromatic aberration and its effect on the measured refractive state

Longitudinal chromatic aberration (LCA) measurements were performed on the optic disk (central retinal artery). This was done because contributions of the reflecting layers in the retina may vary with wavelength and therefore we measured LCA where the multilayer reflection properties of the retina are absent. Average LCA over 9 eyes between three visible wavelengths (457, 514 and 633 nm) and reference wavelength 789 nm (refraction at visible wavelengths minus refraction at 789 nm) are plotted as circle data points in Fig. 5. Measured LCA from 457 nm to 789 nm ranges from 6.2 D to 12.4 D, with an average (± 2 SEM) of

#139905 - $15.00 USD Received 21 Dec 2010; revised 23 Feb 2011; accepted 24 Feb 2011; published 28 Feb 2011
(C) 2011 OSA

10.3 ± 1.3 D. From 457 nm to 633 nm, the average LCA is 7.7 ± 1.0 D. Intersubject variability was higher than measurement variability for all three wavelengths.

In comparison, estimates of the mouse eye LCA using human eye LCA data are also plotted in Fig. 5 (dashed line). In the human eye, LCA from 400 nm to 900 nm were measured experimentally by Thibos et al. and Fernández et al. [25,26]. Using approximations of the water-filled reduced schematic eye, the LCA ratio between different animals equals to the ratio of their total eye power [27]. The ratio of total eye power between the mouse eye and the human eye is ~9.6, thus estimates of the mouse eye LCA would be 9.6 times the human LCA. Since the mouse data is measured with regards to 789 nm, the estimate using human data is also shifted laterally so that LCA is 0 at 789 nm. Figure 5 shows that the measured mouse LCA is in good agreement with estimates using human LCA data.

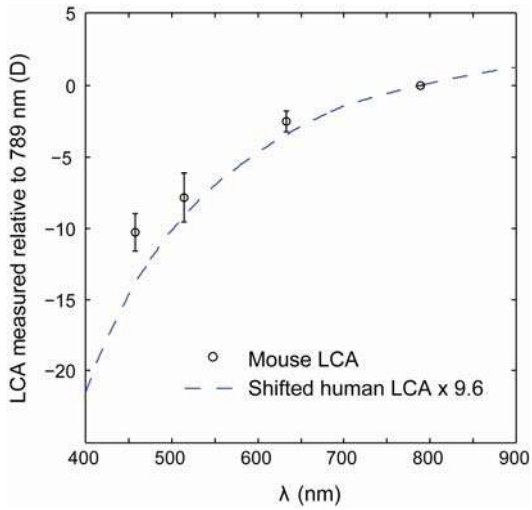

Fig. 5. Experimental data for mouse eye longitudinal chromatic aberration (LCA) and comparisons to theoretical estimates of the mouse eye LCA using human experimental data. Blue dashed lines: estimates of the mouse eye LCA using human LCA data and the water-filled reduced schematic eye. Circle data points: average LCA between wavelengths of 457, 514 and 633 nm, and reference wavelength 789 nm. For example, an average of 10.3 D of chromatic aberration is measured between 457 nm and 789 nm. Error bar: ± 2 SEM.

97% of the mouse photoreceptors are rods and their spectral sensitivity peaks at 497-500 nm [28,29]. Cone photoreceptors are either maximally responsive to UV light (peak sensitivity at 360 nm) or to medium (M)-wavelength light (peak sensitivity at 508 nm) [30]. Compared to the measured refraction at 789 nm, the true refraction would be closer to what would be measured at 514 nm for rods and M cones. The measured average LCA between 514 nm and 789 nm is −7.9 D. Therefore the average refraction at the optic disk for 514 nm would be 13.4 D, and at the outer retina the refractive error would be −15.3 D (for a 2 mm pupil). Chromatic aberration will be even larger between a UV wavelength and 789 nm, thus refraction at the outer retina for UV sensitive cones will be even more myopic. Therefore the mouse eye refraction at the outer retina appears myopic for all the photoreceptor classes.

3.4 Wave aberration of the eye

A typical wavefront sensor spot pattern used for measurement is shown in Fig. 6(a). All images are captured over 2.2 mm pupil sizes and the images are truncated to 2 mm for analysis. Higher order aberration wavefront maps for 6 eyes from 3 mice for a 2 mm pupil size are shown as examples in Fig. 6(b).

#139905 - $15.00 USD Received 21 Dec 2010; revised 23 Feb 2011; accepted 24 Feb 2011; published 28 Feb 2011
(C) 2011 OSA

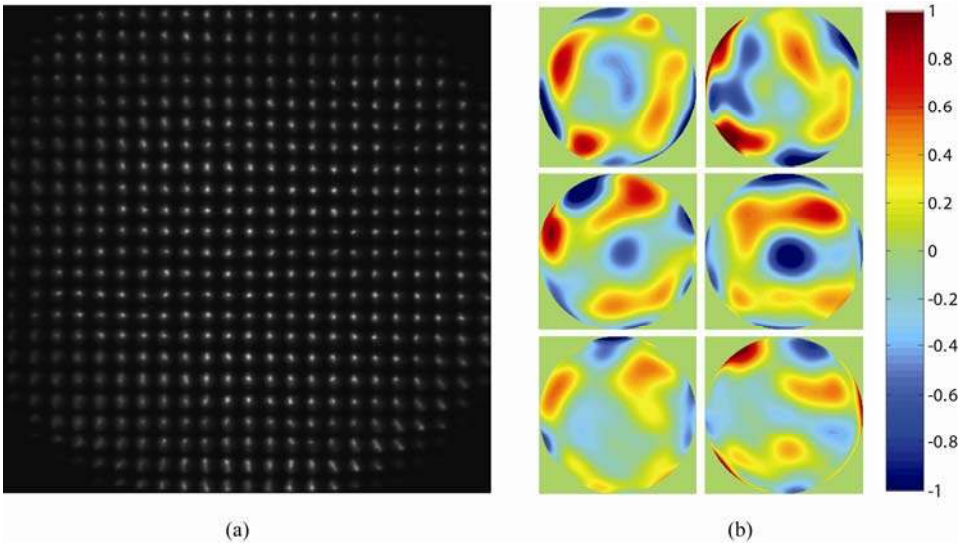

Fig. 6. (a) Typical wavefront sensor spot pattern in the mouse eye used for measurement. Image is captured at 2.2 mm pupil size and wavefront is analyzed at 2 mm pupil size. (b) Higher order aberration wavefront maps for 6 eyes from 3 mice for 2 mm pupil size.

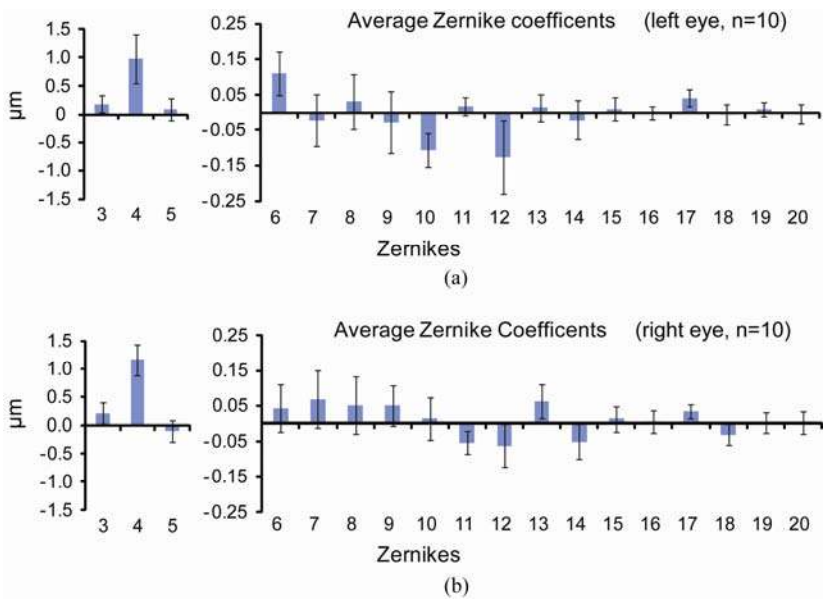

Fig. 7. Mean values of 2nd to 5th order Zernike modes for 20 eyes across a 2 mm pupil, using wavefront spots focused on the outer retina. Zernikes for the 10 left eyes are shown in (a) and ones for the 10 right eyes are shown in (b). Error bars represent ± 2 times SEM. Lower and higher order aberrations are shown using different scales.

The average Zernike coefficients for each mode were calculated in 20 eyes across a 2 mm pupil size using wavefront images focused on the outer retina (Fig. 7). Even though we found indications of correlation between the Zernike coefficients and wavefront maps of the two eyes, we did not find obvious mirror symmetry [31]. Therefore average data from the left eyes and right eyes are shown separately. Lower and higher order aberrations are shown using different scales. Zernike defocus (single index j = 4 or Z_2^0) has the largest magnitude of all the modes. The next largest mode is Zernike spherical aberration (single index j = 12 or Z_4^0),

#139905 - $15.00 USD Received 21 Dec 2010; revised 23 Feb 2011; accepted 24 Feb 2011; published 28 Feb 2011
(C) 2011 OSA

with a value of –0.09 ± 0.06 μm. In comparison, the diffraction-limited RMS for 789 nm wavelength needs to be <0.06 μm (λ/14) according to the Maréchal criterion. Intersubject variability was high for almost all higher order modes. The total root mean square (RMS) wavefront error (± 2 SEM) was 1.28 ± 0.19 μm. The average higher order RMS wavefront errors were 0.38 ± 0.03 μm.

3.5 Strehl ratio and higher order aberrations

These wave aberration measurements can be used to estimate the benefit of correcting the mouse aberrations with adaptive optics. The role of higher order aberrations in reducing the retinal image quality of the mouse eye was assessed by computing the Strehl ratio. Figure 8 shows how the Strehl ratio improves when we successively remove Zernike orders from the wave aberration for a 2 mm pupil. Note that Strehl ratios are calculated for a wavelength of 789 nm, and for visible wavelengths the calculated Strehl ratios will be lower than shown in Fig. 8. Values on the abscissa correspond to the highest Zernike order removed. For the 20 eyes, Zernike orders up to and including 6th order need to be corrected to achieve diffraction-limited imaging (Strehl>0.8) for the 789 nm wavelength. If aberrations are measured using a SHWS and corrected using a deformable mirror, this sets a lower bound for the number of lenslets in the wavefront sensor and the number of actuators in the deformable mirror required to achieve diffraction-limited imaging. The maximum number of Zernike modes that can be reliably reconstructed is approximately the same as the number of lenslets [32]. Since Zernike coefficients up to 6th order correspond to 25 total coefficients without piston, tip and tilt, at least 25 lenslets are needed to recover the important aberrations in the mouse eye. The number of actuators required depends on the type of deformable mirror to be used [32,33].

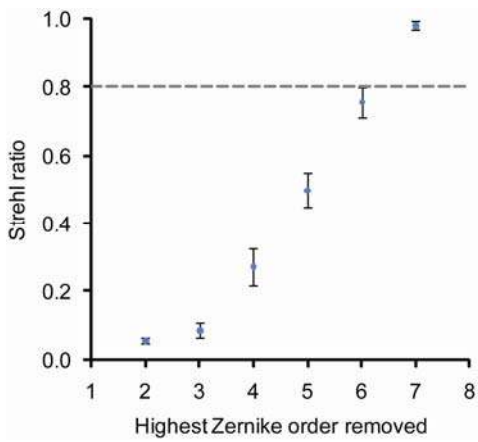

Fig. 8. Strehl ratio for the 20 eyes over a 2 mm pupil at a wavelength of 789 nm. Error bars represent ± 2 SEM. Each data point shows the calculated Strehl ratio after a number of lower order aberrations are corrected. For example, the number 5 means that second, third, fourth and fifth order aberrations (or all aberration modes shown in Fig. 4) are corrected. Dashed line represents a Strehl ratio of 0.8, above which imaging is considered to be diffraction-limited.

3.6 Pupil size, higher order aberrations and modulation transfer functions (MTF)

To determine aberrations present for a pupil size smaller than 2 mm, wave aberrations measured at 2 mm can be truncated and renormalized. Figure 9 shows how the total higher order RMS increases and how the Strehl ratio decreases as the pupil size increases. Note that again Strehl ratios are calculated for a wavelength of 789 nm. Also note that different pupil sizes may include different number of Zernike coefficients, because as the SHWS image is truncated, the number of SHWS spots available in the images is reduced. For pupil sizes larger than 1.4 mm, the aberration coefficients include up to 10th order Zernikes; for smaller pupil sizes, the number of Zernike orders included is reduced. For example, 21 lenslets are

#139905 - $15.00 USD Received 21 Dec 2010; revised 23 Feb 2011; accepted 24 Feb 2011; published 28 Feb 2011
(C) 2011 OSA

included in a 0.6 mm pupil, enough to sample the wavefront up to 5th order Zernikes. For a 0.6 mm pupil size, the higher order RMS is smaller than λ/14, which is considered diffraction-limited according to the Maréchal criterion.

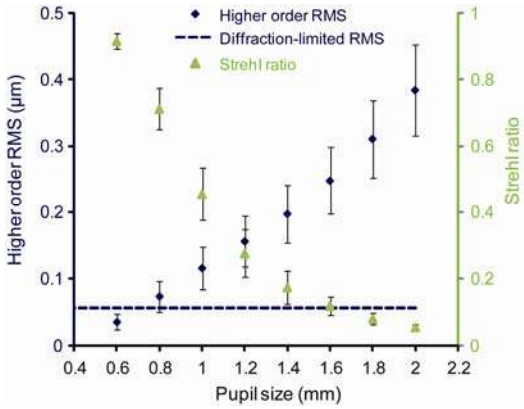

Fig. 9. The total higher order aberration RMS increases, and the Strehl ratio decreases as the eye's pupil size increases. Strehl ratio is calculated for the measurement wavelength of 789 nm. Diamond data points: average measured higher order RMS (3rd to 10th order) in μm. Dashed line: diffraction-limited RMS of λ/14, according to the Maréchal criterion. Triangular data points: average Strehl ratio for each pupil size. Error bars represent ± 2 SEM for the 20 eyes.

Aberrations decrease as pupil size decreases, but the effect of diffraction is larger for smaller pupil sizes. In the human eye, this well known trade off results in a pupil size of 2-3 mm providing the optimum lateral resolution [3,34]. To determine what pupil size will provide the best trade off in the mouse eye, radially-averaged modulation transfer functions (MTFs) were computed using the higher order aberration data in the 20 eyes for different pupil sizes (Fig. 10). At middle and low frequencies, the MTF is the highest for a 0.8 mm pupil size, where the MTF is close to diffraction-limited. However, larger pupil sizes provide better modulation transfer at the very highest spatial frequencies that only these large pupils can pass at all.

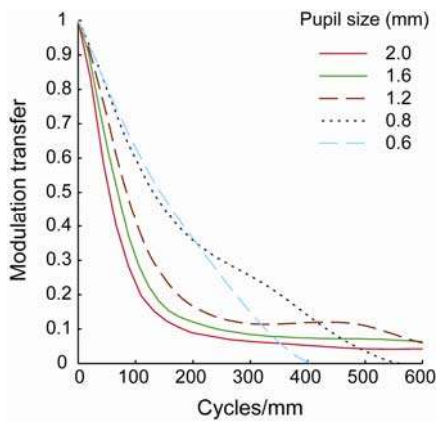

Fig. 10. Mean of radial averaged MTF for 20 eyes over different pupil sizes (0.6 mm to 2 mm) for the measurement wavelength of 789 nm. Defocus and astigmatism are removed before MTF is calculated.

3.7 Comparison between MTF of the human eye and the mouse eye

The average mouse eye MTF was compared with the average MTF computed from higher order aberration measurements obtained in 378 healthy normal human eyes over a 6 mm pupil

#139905 - $15.00 USD Received 21 Dec 2010; revised 23 Feb 2011; accepted 24 Feb 2011; published 28 Feb 2011
(C) 2011 OSA

size [35]. The human higher order aberration data were measured up to and including 5th order Zernike polynomials. To characterize the angular resolution of the eye viewing the world, the MTF was plotted in cycles/degree (Fig. 11(a)). The mouse eye has a lower diffraction-limited MTF for angular resolution than the human eye as expected. Based on higher order aberrations, the mouse eye and the human eye MTF drop from the diffraction-limited MTF in a similar way, and the human eye modulation transfer is higher than that of the mouse eye for all frequencies. To characterize the spatial resolution when an investigator is viewing the retina, the MTF was plotted in cycles/mm. This way, eyes with higher NAs have larger diffraction-limited MTFs, and eyes with the same NA share the same diffraction-limited MTFs despite their differing pupil sizes and focal lengths. Figure 11(b) shows that the mouse eye has a better diffraction-limited MTF in cycles/mm than the human eye due to its larger NA. Even with higher order aberrations present, the mouse eye still has a higher modulation transfer for all the spatial frequencies expressed in cycles/mm than the human eye.

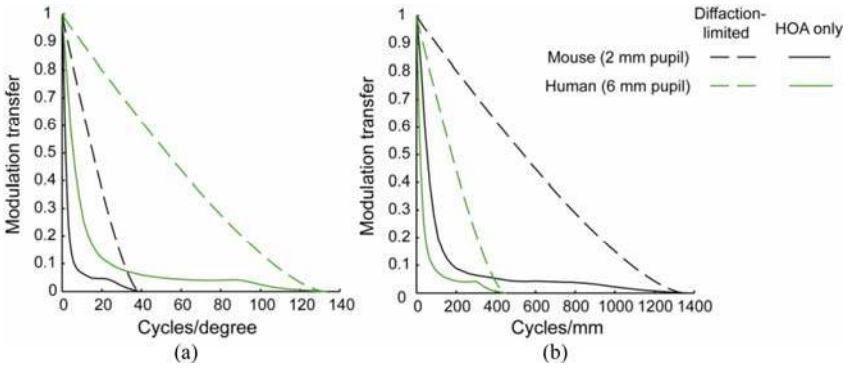

Fig. 11. Modulation transfers for a human eye (6 mm pupil) and a mouse eye (2 mm pupil) plotted in (a) cycles/degree to characterize angular resolution for vision and (b) cycles/mm to characterize spatial resolution for imaging the retina. Only higher order aberrations (HOA) are considered. Solid black line: mouse eye with 2 mm pupil size with HOA. Solid green line: human eye with 6 mm pupil size with HOA. Dashed black line: Diffraction-limited mouse eye with 2 mm pupil size. Dashed green line: Diffraction-limited human eye with 6 mm pupil size.

3.8 Simulated retinal images

The high spatial resolution in the mouse eye as shown in Fig. 11(b) provides the potential of achieving even higher resolution retinal images than can be obtained in the human eye. To simulate retinal images of fluorescent ganglion cells, a fluorescent ganglion cell from a flat-mounted rat retina imaged with confocal microscopy with 1.2 NA is used as the original image [Fig. 12(a)]. Note that simulation used aberration data measured with 789 nm wavelength; if imaging is performed using shorter wavelength, image degradation will be worse with aberrations, and the benefit of AO correction will be greater. For imaging without AO, after focus and astigmatism is corrected, Fig. 10 shows that 0.8 mm pupil gives the best MTF for low to middle spatial frequencies. For a 0.8 mm pupil size, the higher order aberration RMS for a typical eye is only 0.07 μm. Figure 12(b) shows the simulated best ganglion cell image obtained without AO over a 0.8 mm pupil. Even though image contrast is reduced, all the ganglion cell bodies and most of the axons and dendrites can be resolved. Figure 12(c) shows the same cells imaged with ideal AO correction over a 2 mm pupil size with increased contrast. Figure 12(d)-(f) shows the same simulation for incoherent imaging of rods. The rod image in Fig. 12(d) is a simulated triangularly packed mosaic [36] with a nearest neighbor distance of 1.6 μm (calculated using average rod density [28]). For the rod image, if imaged without AO using a 0.8 mm pupil (Fig. 12(e), the spatial frequency corresponding to the average rod spacing is already beyond the cut off frequency of the optics. Here the improvement afforded by AO is critical to resolve individual cells.

#139905 - $15.00 USD Received 21 Dec 2010; revised 23 Feb 2011; accepted 24 Feb 2011; published 28 Feb 2011
(C) 2011 OSA

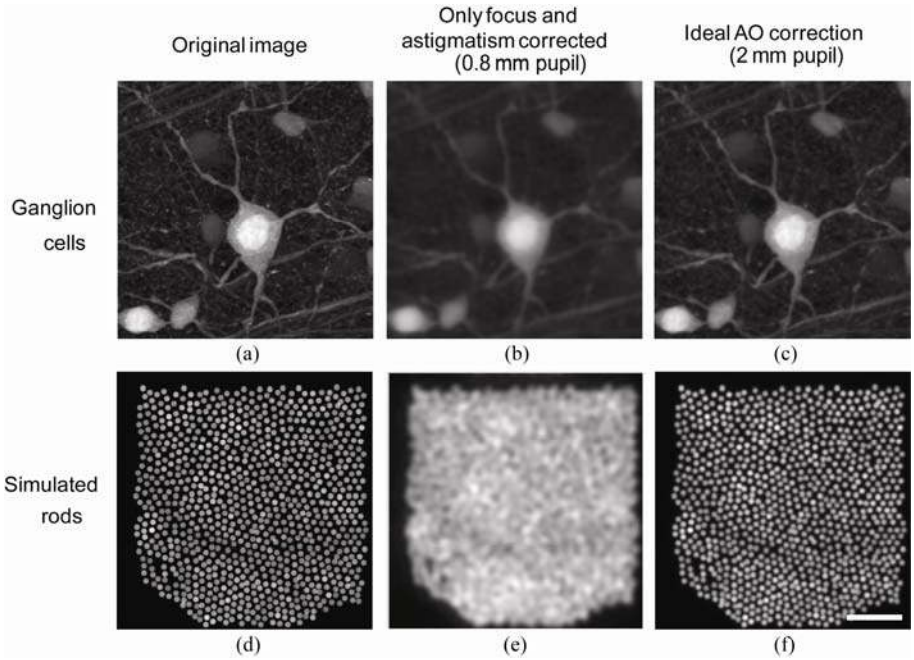

Fig. 12. Simulated retinal images of ganglion cells and rod photoreceptors under ideal imaging conditions and in the absence of noise with/without AO correction. (a) A fluorescent ganglion cell image from a flat-mounted rat retina imaged with confocal microscopy with 1.2 NA. (b) A simulation of the retina in (a) being imaged without AO correction over a 0.8 mm pupil under the best possible condition. (c) A simulation of the same ganglion cell being imaged with AO correction over a 2 mm pupil under the best possible condition. (d) A simulated rod photoreceptor mosaic in the mouse retina. (e) & (f) are the same without AO and with AO simulations of the rod photoreceptor mosaic. Scale bar: 20 μm.

4. Discussion

4.1 Method for measuring the wave aberration

Measuring the wave aberration of the mouse eye with a replica of the method used in the human eye is difficult due to the severely degraded Shack-Hartmann spots [13]. The current study suggests that the origin of the degraded spot pattern lies in the multiple back reflections from the optically thick retina, instead of imperfections such as higher order aberrations present in the mouse eye optics. By carefully controlling the beacon focus, our wavefront sensor spots shown in Fig. 3(c) and 3(d) provide good quality approaching the diffraction-limit. This wavefront sensor that favors backscattered light from a specific retinal layer improves the wavefront spot image quality and hence aberration measurements in the mouse eye. Another method that may be worth exploring for wavefront sensing in the mouse eye on a particular layer is to utilize coherence [37].

Even though according to Eqs. (1) and (2), the elongation of the wavefront spots in the human eye caused by the retinal thickness is a lot smaller than that in the mouse, it would be interesting to find out if this would affect the wavefront sensing accuracy in the human eye, especially at eccentricities with thicker nerve fiber layer and larger overall thickness. This will probably be a small effect, but it has been observed during AOSLO imaging of the human retina that the wavefront sensor is sometimes confused, locking on the nerve fiber layer instead of on the photoreceptor layer [38].

4.2 Refractive error and the small eye artifact

As one would expect, we measured different refractive errors when the wavefront sensor beacon was focused on different layers and at different retinal eccentricities. The average

#139905 - $15.00 USD Received 21 Dec 2010; revised 23 Feb 2011; accepted 24 Feb 2011; published 28 Feb 2011
(C) 2011 OSA

equivalent sphere values are + 21.9 D hyperopic when the beacon is focused on the optic disk and −7.4 D myopic when focused on the outer retina for 789 nm wavelength. The refraction value on the optic disk (central retinal artery) was further confirmed by the ~20 D of trial lens focus needed on the fundus camera for the disk to be in focus. This is consistent with the so called "small eye artifact" in retinoscopy [39], in which the true measured refraction is confounded by reflection from a retinal layer different from the photoreceptor layer. The small eye artifact is especially pronounced in eyes where the retinal thickness is large relative to the effective focal length of the eye. It has been calculated that the dioptric difference of the positions from the vitreo-retinal interface (where the retinoscopic reflection is supposed to originate [39]) to the RPE for the adult C57BL/6 mice is ~39 D [2]. The dioptric difference we measured from the optic disk to the outer retina was 29.2 D and lies within the total optical thickness of the retina.

All previous studies provided hyperopic readings for the the mouse eye. However, with the confounding small eye artifact, the true refraction is likely to be less hyperopic than reported [1,2]. Our measurements indicate that the real refraction for the mouse eye is probably myopic. White light streak retinoscopy studies have found + 13.5 D to over + 15 D of hyperopia [39–41]. An IR photoretinoscopy study found about + 7 D of hyperopia [2], and finally the previous Shack-Hartmann study found + 9.7 D of hyperopia [13].

In the present study, we also observed hyperopic refractions in the case where the beacon was focused on the central retinal artery located on the optic disk. The OCT image in Fig. 3(c) shows that the central retinal artery is highly reflective and lies at a depth that is close to that of the vitreo-retinal interface. In that case, taking into account the measured chromatic aberration of the mouse eye, the average refraction at the disk (central retinal artery) for 514 nm was calculated to be 13.4 D for a 2 mm pupil, or 15.3 D for a 0.8 mm pupil. This value is consistent with retinoscopy results, suggesting that the retinoscopic reflection is probably generated from the vitreo-retinal interface as suggested by Glickstein [39]. Both the IR photoretinoscopy study [2] and the previous SHWS study [13] measured a value between our 21.9 D hyperopia for the inner retina (central retinal artery) and −7.4 D myopia for the outer retina. Our result may be consistent with those results if the signal they measured is a weighted average from different retinal layers.

To estimate the true refraction of the mouse eye, the average refraction at the outer retina was calculated to be quite myopic at −15 D for a wavelength of 514 nm (that is, in which the chromatic aberration has been taken into account). In the mouse, the available evidence seems to suggest that the most reflective layer in the outer retina may lie deeper than the photoreceptor, in the RPE and choroid [22,23]. If the spot centroid lies on the RPE or choroid instead of the photoreceptor layer, the true refraction would be less than −15 D, but would still be myopic. This is the first study that indicates the mouse eye may be myopic. It would make sense for the animal to be myopic or emmetropic, since for a hyperopic eye, no object vergence will give a sharp image on the retina. With a large depth of field of at least ± 11 D [1], even with very myopic eyes the mouse should still be able to achieve reasonable focus for far objects.

Our mice were anesthetized and it is not clear how much anesthesia affects measured refraction. It was reported that in one mouse eye, the hyperopic spherical equivalent was reduced by 7 D in the anesthetized eye [13]. However, a recent photorefraction study measured the opposite effect, that ketamine–xylazine anesthesia caused on average 6.9 D of hyperopic refractive shift in 9 mice eyes [42]. Another retinoscopy test of five *C57BL/6J* mice measured no difference larger than ± 2 D in the same eyes between awake vs. anesthetized state (Marsha L. Kisilak, unpublished data). In any case, a focal shift in the range of −7 D to 7 D to the anesthetized refractive state of −15 D will not render the mouse eye hyperopic.

4.3 Chromatic aberration

To our knowledge this is the first *in vivo* measurement of the mouse eye chromatic aberration. The current *in vivo* measurement and previous estimations of the mouse eye chromatic

#139905 - $15.00 USD Received 21 Dec 2010; revised 23 Feb 2011; accepted 24 Feb 2011; published 28 Feb 2011
(C) 2011 OSA

aberration are summarized in Table 2. Remtulla and Hallett developed a homogeneous schematic eye from measuring frozen mouse eye sections [1]. With refractive indices measured at 4 wavelengths and paraxial ray tracing, they estimated a chromatic aberration of 20.2 D (13-20 D) between 488 nm and 655 nm. In contrast, we measured only 7.7 D ± 1.0 D (mean ± 2SEM) chromatic aberration between 457 nm and 633 nm. Except for experimental uncertainties, we are not sure about the origins of the large difference between this schematic eye and our result. Even though schematic eye studies assume a narrow paraxial beam while we experimentally measured the aberrations over a fully dilated pupil, our refraction measurements in a 2 mm and 0.8 mm pupil size (Fig. 4) didn't show much change. The water-filled reduced schematic mouse eye model gives 8.8 D for the same wavelength range as the current study using total eye power values from Remtulla and Hallet [1,27], which agrees very well with our experimental value.

If the only significant difference between mouse and rat eyes is a linear scale difference of two times, the mouse eye chromatic aberration should be two times as large as that of the rat eye. Similar to the mouse schematic eye, Chaudhuri et al. had a rat homogeneous model eye measured from enucleated eyes and their estimation for chromatic aberration was 5.8 D between 486 nm and 656 nm [43]. Our measured value (7.7 D) is closer to two times the value from the Chaudhuri et al. rat schematic eye model (11.6 D) than the mouse schematic eye value (20.2 D). There had also been retinoscopy measurements using relatively broad-band red and blue light, and their estimated rat eye LCA was 2.5-3.5 D [44,45]. Our result is consistent with a value that is roughly two times the rat eye retinoscopy results (5.0 D – 7.0 D).

Table 2. Current *in vivo* measurement and previous estimations of the mouse eye chromatic aberration

	Rat eye × 2		**Mouse eye**		
	Schematic eye from measuring frozen sections [43]	Retinoscopy [44,45]	Schematic eye from measuring frozen sections [1]	Water-filled schematic eye [27]	Current study
Wavelength Range (nm)	486–656	Broadband blue to red	488–655	457–633	457–633
Chromatic Aberration	11.6 D	5.0–7.0 D	20.2 D (13–20 D)	8.8 D	7.7 ± 1.0 D

4.4 Comparison of measured higher order aberrations and MTF with other studies

The magnitude of higher order aberrations measured in anesthetized mice in this study is smaller than that measured in awake behaving mice by de la Cera et al. [13]. If the measured data in this study is cropped to 1.5 mm pupil size and includes only up to 4th order Zernikes, the average RMS higher order aberration is 0.20 ± 0.05 μm (mean ± standard deviation) compared with 0.32 ± 0.08 μm reported previously [13]. The average spherical aberration measured in this study is negative, but with a large variability, compared to a measured larger positive spherical aberration of 0.15 ± 0.06 μm reported previously. If mice being used are genetically identical, there are several possible explanations for the differences in the magnitude of higher order RMS. Different wavefront spot quality and centroiding algorithms could affect the final measurement. Anesthetized mice may have different aberrations compared with awake mice however awake mice may have better optical quality, as indicated in studies done in mice and cats [13,46]. The eccentricities at which wave aberrations are being measured can be different. Last but not least, depending on the different contribution to the wavefront spots from various retinal layers, aberrations measured can be different.

IR photorefraction in the mouse eye typically show non-uniform intensity distributions with ring-shaped areas in the pupil [47]. This pattern is different from the smooth pupil illumination pattern observed in human eyes using the same technique [48]. It is possible that higher order aberrations contribute to this non-uniform intensity, even though we did not find

#139905 - $15.00 USD Received 21 Dec 2010; revised 23 Feb 2011; accepted 24 Feb 2011; published 28 Feb 2011
(C) 2011 OSA

the mouse eye higher order aberrations to be significantly larger than that of the human eye. As was described in 3.1, the mouse eye SHWS spot intensity on the pupil is non-uniform and contains reflections from multiple layers in the retina, some of which having a specular reflection component. These reflections are also eccentricity dependent, with an especially bright reflection coming from the central retinal artery. We do not know whether these non-uniformities have an impact on other methods of measuring the eye's optics, such as IR photorefraction. Geometrical theory to predict eccentric photorefraction intensity profiles assumes a single retinal layer which diffusely scatters light, with reflection properties independent of eccentricity [49,50]. It might be possible that the multilayer properties of the mouse retina may also contribute to the non-uniform intensity distribution observed during IR photorefraction.

Artal et al. calculated the MTF for a single mouse eye using a double-pass method and found the modulation to be lower than 0.1 for 1 cycle/degree for a 1 mm pupil [10]. Our data gives a modulation of above 0.5 for the same frequency and pupil size for an average of 20 eyes even before defocus and astigmatism are removed, and a modulation of above 0.8 when defocus and astigmatism are removed. Our MTF is significantly higher than that measured using the double-pass method. However, comparisons of double-pass and wavefront sensor MTFs are complicated by the failure of the wavefront sensor to capture scatter, and the possibility that the double-pass method exaggerates the effect of scatter. Following the lower higher order RMS, the calculated MTF in this study is also slightly higher than previous results obtained using Shack-Hartmann wavefront sensor [13].

4.5. Optical and neural factors in mouse spatial vision

The visual acuity of the mouse is only 0.5-0.6 cycles/deg [51,52], about a factor of 100 worse than human. The optics of the mouse eye could support substantially higher visual acuity than this. We have found that a pupil size of 0.8 mm provide the best MTF for low and middle spatial frequencies (Fig. 10). Figure 13 shows that for a 0.8 mm pupil and 514 nm wavelength, when both lower and higher order aberrations are taken into account, the modulation transfer is ~0.6 for the maximum acuity of 0.6 cycles/deg, indicating that optics is not the limiting factor for mouse vision.

The rod Nyquist limit in the mouse is 9.5 cycles/deg (calculated using average rod density data from Jeon et al. assuming triangular packing [28]). The visual acuity is, not surprisingly, much lower than that expected from the rod mosaic. Presumably, as in the human, the mouse rod mosaic pools photons over many rods to increase the signal-to-noise ratio at low light levels. However, different from the human eye, mouse eye spatial vision seems to be governed by rods instead of cones. It has been shown that knock-out mice with only rods have normal grating acuity, but mice with only cones have much worse than normal acuity [53]. At the rod Nyquist limit, Fig. 13 shows that when all aberrations are present, the average modulation transfer for an eye with 0.8 mm pupil is at ~0.02. This is a conservative estimate since the defocus values used assumes fixation at infinity. For an object closer to the mouse which it is probably more interested in, the myopic mouse could have a modulation as high as 0.12 (if defocus is excluded from MTF calculations). The MTF is sufficiently reduced at the rod Nyquist limit that there is essentially no risk of aliasing.

The cone Nyquist limit in the mouse is 1.6 cycles/deg (also calculated using density data from Jeon et al. assuming triangular packing [28]). At 1.6 cycles/deg, Fig. 13 shows that even when all aberrations are present, the average modulation transfer for an eye with 0.8 mm pupil is 0.25. For an object closer to the mouse, the myopic mouse could have a modulation as high as 0.75 for the cone Nyquist limit. Therefore cones undersample the mouse retinal image, unless there are additional major degradations to the image quality not accounted for, such as scattering.

Similarly the ganglion cell Nyquist limit (even if we assume that each cell independently samples the retinal image) is 0.9-1.3 cycles/deg [28,54,55], which undersamples the retinal image even more than the cones do. If only a subset of the total ganglion cell population is used for behavioral acuity, that subset could set the resolution limit for the mouse.

#139905 - $15.00 USD Received 21 Dec 2010; revised 23 Feb 2011; accepted 24 Feb 2011; published 28 Feb 2011
(C) 2011 OSA

Alternatively, additional high frequency loss caused by ganglion cell receptive field size or from more central stages in the mouse visual pathway might account for the poor behavioral acuity of the mouse.

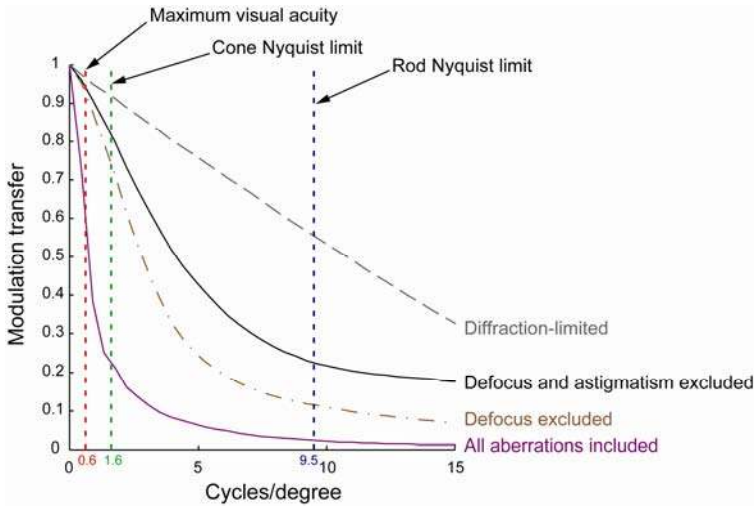

Fig. 13. Average modulation transfer functions for the mouse eye over a 0.8 mm pupil diameter. Note that MTFs are calculated for a wavelength of 514 nm, where rods and M-cones are near their spectral sensitivity peak.. To calculate MTF for a visible wavelength using wave aberration data measured at 789 nm, we assume other than defocus, variations in the other aberration coefficients between visible and IR wavelengths are small [26,56]. For all 20 eyes, defocus was increased by 7.9 D based on measured average LCA between the two wavelengths and Zernike coefficients for other aberrations remained the same.

In any case, the mouse eye optics is very good with respect to the retinal sampling properties and the behavioral performance of the entire animal. It may be that the optical quality of the mouse eye has evolved to be as good as it is to ensure high contrast at the very low frequencies that the nervous system is sensitive to. This relationship is consistent with observations in vertebrates that the optical quality of the eye tends to outperform the sampling limitations imposed by the retina, especially in animals that live in dim light [57–59]. One such example is the barn owl, which has almost diffraction-limited optics and an axial length not much smaller than the human eye (17.5 mm), but with a behavioral acuity of only about 4 cycles/degree [60,61].

4.6 Optical quality of the mouse eye: visual performance vs. retinal imaging

A comparison of the optical quality of the human and mouse eye depends on whether the basis for the comparison is the organism's visual performance or the experimenter's ability to resolve structure in the retina. For a scene that subtends a certain visual angle, the small mouse eye can only use a very small size retina to sample the scene and thus is at a clear disadvantage. The MTF expressed in cycles per deg in Fig. 11(a) shows that the human optics can support better visual performance than the mouse optics can.

On the other hand, the NA of the dilated mouse eye is approximately two times larger than the dilated human eye, presumably because the increase in light gathering power benefits the nocturnal mouse. From the point of view of retinal imaging, this larger NA makes it theoretically possible to image anatomical structures in the mouse retina that are half the size of the smallest feature that can be resolved in the human eye. When higher order aberrations are taken into account, and for the case of imaging the retina rather than visual performance, the mouse still outperforms the human eye as shown in Fig. 11(b). This runs counter to the view that mice have large amounts of higher order aberrations and encourages the prospects for resolving cellular structures in the rodent retina even without AO.

#139905 - $15.00 USD Received 21 Dec 2010; revised 23 Feb 2011; accepted 24 Feb 2011; published 28 Feb 2011
(C) 2011 OSA

4.7 Adaptive optics retinal imaging in the mouse eye

With the remarkably good optical quality of the mouse eye for imaging the retina, it's possible to obtain high quality retinal images even without using AO [62–65]. However AO can provide additional improvements in both lateral and axial resolution and retinal image contrast. The diffraction-limited *in vivo* resolution is ~0.7 µm for lateral resolution, and ~6 µm for axial resolution (calculated for 550 nm wavelength and 2 mm pupil size). Apart from providing diffraction-limited imaging, AO can also increase the pupil size that can be used for imaging, correct both lower and higher order aberration at video rates, and increase light collection efficiency for confocal or two-photon imaging. The ability to capture the entire wave aberration in the anesthetized mouse eye over a fully dilated pupil with reflected light is promising for high-speed adaptive correction of mouse retinal images. The amount of higher order aberrations measured over the 0.49 NA (2 mm pupil) mouse eye is similar to what is measured in the normal human eye over a 0.18 NA (6 mm pupil) [66] thus is correctible by AO. An adaptive optics instrument customized for *in vivo* imaging of the mouse retina with this improved wavefront sensing method is currently under development.

5. Conclusions

Using a wavefront sensor that favors backscattered light from a specific retinal layer in the mouse eye, we have improved the quality of wavefront sensor spots and thus improved aberration measurements in the mouse eye. Contrary to common belief, we measured the mouse eye to be myopic, and the optical quality of the mouse eye to be remarkably good. An instrument constructed with this improved wavefront sensor technique may provide a faster and more effective correction for the mouse eye aberrations using AO. This instrument can potentially achieve a lateral resolution at least two times higher than that of the human eye, and an axial resolution at least four times higher than that of the human eye. Such an instrument could allow microscopic imaging and monitoring of retinal development, disease progression, or the efficacy of therapy in single animals over time.

Acknowledgments

We appreciate financial support from the following sources: NIH Grants EY 001319, EY014375, EY018606, NSF STC grant No. AST-9876783, and Research to Prevent Blindness. Alfredo Dubra-Suarez, PhD, holds a Career Award at the Scientific Interface from the Burroughs Wellcome Fund. Richard T. Libby holds a Research to Prevent Blindness Career Development Award. We thank Wanli Chi, Jennifer Hunter, Sonia Luther, Lu Yin, Benjamin Masella, Jason Porter, Marsha Kisilak, Ramkumar Sabesan, Boshen Gao, William Merigan, Geunyoung Yoon, William Fisher and Nicole Putnam for their assistance on this work. We would also like to thank the reviewers for providing valuable comments and suggestions for the manuscript.